SCIENTIFIC REPORTS

OPEN

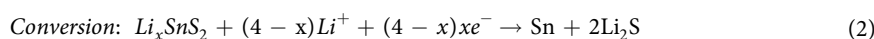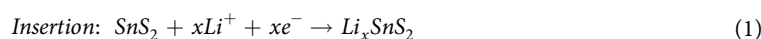# Unlocking the potential of SnS$_2$: Transition metal catalyzed utilization of reversible conversion and alloying reactions

Zhi Xiang Huang[1,2], Ye Wang[1], Bo Liu[1], Dezhi Kong[1], Jun Zhang[3], Tupei Chen[3] & Hui Ying Yang[1]

The alloying-dealloying reactions of SnS$_2$ proceeds with the initial conversion reaction of SnS$_2$ with lithium that produces Li$_2$S. Unfortunately, due to the electrochemical inactivity of Li$_2$S, the conversion reaction of SnS$_2$ is irreversible, which significantly limit its potential applications in lithium-ion batteries. Herein, a systematic understanding of transition metal molybdenum (Mo) as a catalyst in SnS$_2$ anode is presented. It is found that Mo catalyst is able to efficiently promote the reversible conversion of Sn to SnS$_2$. This leads to the utilization of both conversion and alloying reactions in SnS$_2$ that greatly increases lithium storage capability of SnS$_2$. Mo catalyst is introduced in the form of MoS$_2$ grown directly onto self-assembled vertical SnS$_2$ nanosheets that anchors on three-dimensional graphene (3DG) creating a hierarchal nanostructured named as SnS$_2$/MoS$_2$/3DG. The catalytic effect results in a significantly enhanced electrochemical properties of SnS$_2$/MoS$_2$/3DG; a high initial Coulombic efficiency (81.5%) and high discharge capacities of 960.5 and 495.6 mA h g^{-1} at current densities of 50 and 1000 mA g^{-1}, respectively. Post cycling investigations using *ex situ* TEM and XPS analysis verifies the successful conversion reaction of SnS$_2$ mediated by Mo. The successful integration of catalyst on alloying type metal sulfide anode creates a new avenue towards high energy density lithium anodes.

The relentless growth of modern technology is constantly feeding society's increasing need for energy usage and consumption. However, the development of energy storage devices has not been able to keep pace with the rapid progress of portable electronics, large-scale usage such as Electric Vehicles (EVs), plug-in hybrid Electric Vehicles (PHEV) and even grid-scale storage[1-3]. Over the course of developing an effective anode material, tin-based anode materials has been recognized as one of the most promising materials to replace the current generation of commercial graphite anode[4-6]. This is due to its salient features such as high theoretical capacity, high energy density owing to low voltage discharge profile and low cost due to its high abundance in nature[6,7]. Amongst the different tin-based anode materials, SnS$_2$ offers a two-dimensional layered type structure where the CdI$_2$-type layers are loosely bounded by weak van der Waals forces and hence easily susceptible to the intercalation of lithium-ions (Li$_x$SnS$_2$)[8,9]. Further interaction with lithium-ions in a discharge process results in the conversion process of the lithiated SnS$_2$ to form metallic Sn and Li$_2$S[8,10]. In subsequent charge-discharge cycles, the liberated tin alloys reversibly with lithium forming Li$_{4.4}$Sn. The above reactions can be described using the following equations:

$$Insertion: \; SnS_2 + xLi^+ + xe^- \rightarrow Li_xSnS_2 \tag{1}$$

$$Conversion: \; Li_xSnS_2 + (4-x)Li^+ + (4-x)xe^- \rightarrow Sn + 2Li_2S \tag{2}$$

Simplifying equations (1) & (2),

[1]Pillar of Engineering Product Development, Singapore University of Technology and Design, 8 Somapah Road, Singapore 487372, Singapore. [2]Airbus Group Innovations Singapore, 110 Seletar Aerospace View 797562, Singapore. [3]School of Electrical and Electronic Engineering, Nanyang Technological University, Singapore 639798, Singapore. Correspondence and requests for materials should be addressed to H.Y.Y. (email: yanghuiying@sutd.edu.sg)
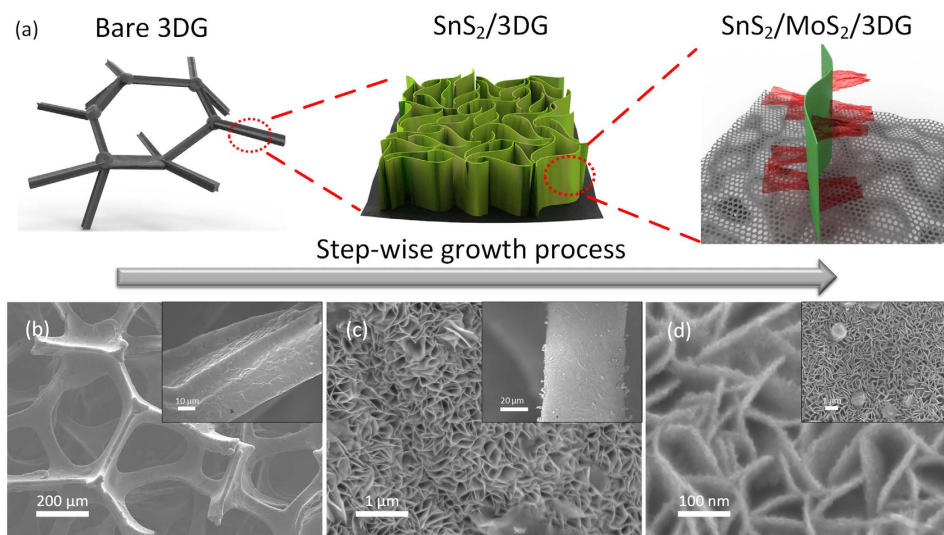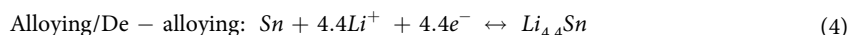
Figure 1. (**a**) Illustration of the growth process of SnS$_2$/MoS$_2$/3DG via stepwise solvothermal synthesis. In increasing high and low (inset) magnification SEM images of (**b**) pristine etched 3DG, (**c**) SnS$_2$/3DG, and (**d**) SnS$_2$/MoS$_2$/3DG.

$$SnS_2 + 4Li^+ + 4e^- \rightarrow Sn + 2Li_2S \qquad (3)$$

In subsequent charge-discharge cycles,

$$\text{Alloying/De} - \text{alloying:} \quad Sn + 4.4Li^+ + 4.4e^- \leftrightarrow Li_{4.4}Sn \qquad (4)$$

The reversible reaction of Sn in SnS$_2$ with 4.4 mols of lithium (equation (4)) translates into a high theoretical capacity of 645 mAh g^{-1} (compared to graphite: 372 mAh g^{-1}). Despite this, it can be observed that 4 mols of lithium is spent in the irreversible formation of Li$_2$S during the conversion reaction of lithiated SnS$_2$ (equation 2). Hence, the theoretical capacity of SnS$_2$ can potentially be as high as 1231 mAh g^{-1} (8.4 mol Li$^+$ per mol SnS$_2$) compared to 645 mAh g^{-1} (4.4 mol Li$^+$ per mol SnS$_2$) if the irreversible reaction in equation 2 is made reversible.

To date, there are several reports of SnS$_2$ with beyond theoretical capacities of 645 mAh g^{-1} [11–23]. However, the origin of these excess capacities are often unclear and attributed to the effects of nano-sized SnS$_2$ and possible synergistic effects with carbonaceous materials such as amorphous carbon[11,12], carbon nanotubes[13,24], and reduced graphene oxides[14–20,25]. The synthesis and formation of nanostructures and nanocomposites is a common strategy to overcome large volume changes that SnS$_2$ experience during lithiation and delithiation that plagues the stability and cyclability of the active material. The carbonaceous materials within the nanocomposite does not only provide volume change buffers for SnS$_2$, but also serves to improve electron conduction. These strategies are also common to transition metal oxides and sulfides based anode materials[26–30]. However, efforts have been limited to the above strategies and little has been done to properly utilize both conversion (equation 2) and alloying (equation 4) process of SnS$_2$, which can potentially improve capacities significantly.

Herein, we present the successful integration of a small amount of Molybdenum (Mo) nanoparticles catalyst, directly onto Sn$_2$ nanosheets, to promote the active reversible conversion process of Sn to SnS$_2$ and decomposition of Li$_2$S. Mo catalyst, grown onto SnS$_2$ in the form of MoS$_2$, leads to a remarkable enhancement in the performance of the lithium ion ion batteries. Furthermore, SnS$_2$ nanosheets are grown onto 3-dimensional graphene foam (3DG) to improve conductivity and suppress volume changes during charge and discharge cycles. The as-synthesized SnS$_2$/MoS$_2$/3DG are directly used as binder-free and lightweight electrodes where it exhibits enhanced electrochemical performance in terms of improved specific capacity, high rate capability and cycling stability. Direct evidence of the catalytic effect of Mo is also observed via *ex situ* transmission electron microscopy (TEM) and X-ray photospectroscopy (XPS) analysis. This catalytic process is able to overcome the irreversible reaction in the tin-based anode materials and has important implications for future applications for such materials in various energy storage systems.

Results and Discussion

Characterization of Materials. The step-by-step synthesis process and morphology of SnS$_2$/MoS$_2$/3DG nanostructure is detailed in the illustration and the corresponding SEM images in Fig. 1. 3DG was prepared by CVD using ethanol as carbon source and Ni foam as a substrate. The Ni foam substrate was subsequently etched away using 3 M HCl leaving a lightweight 3DG current collector ($\sim$0.5 mg cm^{-2}) (Fig. 1b). SnS$_2$ nanosheets ($\sim$1.2 mg cm^{-2}) were uniformly grown onto 3DG through a facile solvothermal synthesis process where surfactant (SDS), was used to reduce the size of the nanosheet (Fig. 1c)[31,32]. This creates a denser loading of SnS$_2$ on 3DG (Figure S1, see Supporting Information). In the second solvothermal synthesis step, trace amounts of MoS$_2$ precursors were used to control the limited growth of MoS$_2$ catalyst on SnS$_2$. This was carried out by
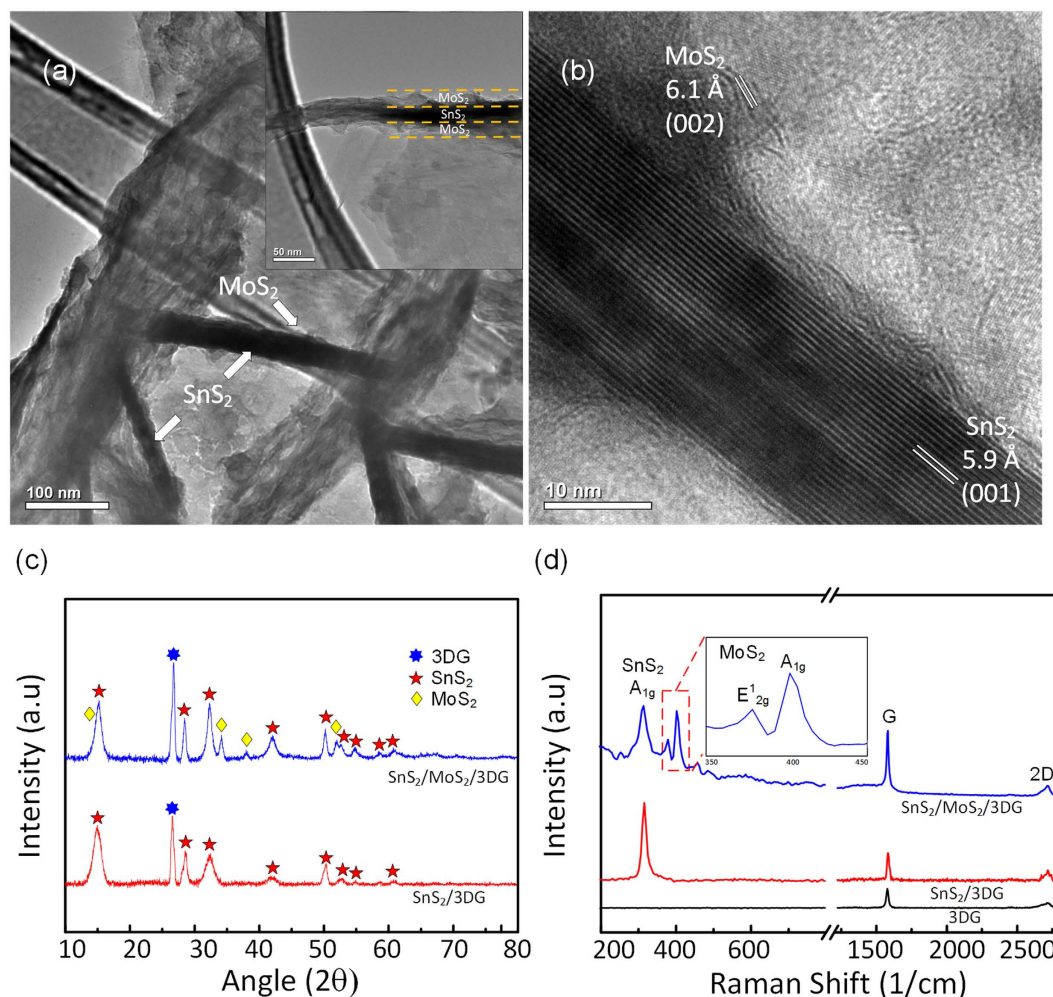
Figure 2. HRTEM images of SnS_2/MoS_2/3DG (**a**) low magnification with inset showing sandwich MoS_2/SnS_2/MoS_2 and (**b**) high magnification showing lattices of SnS_2 and MoS_2. (**c**) XRD pattern of SnS_2/MoS_2/3DG and SnS_2/3DG. (**d**) Raman spectra of SnS_2/MoS_2/3DG, SnS_2/3DG, and as-prepared 3DG.

placing pieces of the as-synthesized SnS_2/3DG in the Teflon-lined autoclave with the dissolved MoS_2 precursors. As shown in Fig. 1d, sparse amount of MoS_2 nanosheets were grown directly onto the surfaces of SnS_2 nanosheets. Instead of directly introduction Mo as a catalyst, MoS_2 nanosheets were grown on SnS_2 to exploit the 2D nature of MoS_2 with large exposed surfaces that will facilitate rapid catalytic action during charge-discharge cycles. Lastly, ethanol solvent was used in both solvothermal syntheses as 3DG is hydrophobic. The final product, SnS_2/MoS_2/3DG, can be used directly as a lightweight binder-free anode material without needing additional conductive carbon. Figure S2 shows a photograph of the as-synthesized products where the stepwise growth of the SnS_2 and MoS_2 results in a color change of the electrode, green (SnS_2) then black (MoS_2). In order to obtain a more detailed morphology of MoS_2 growth on SnS_2, TEM characterization was carried out as shown in Fig. 2a,b. From the TEM image in Fig. 2a, fine sheets of MoS_2 can be clearly observed on both sides of the larger SnS_2 nanosheets. This sandwich structure is clearly marked out as shown in the inset of Fig. 2a. In the high resolution TEM image in Fig. 2b, the interplanar spacing of 6.0 Å and 5.8 Å can be assigned to the (002) and (001) crystal planes of MoS_2 and SnS_2 respectively[8,28].

The crystalline phases and structures of the as-synthesized SnS_2/3DG and the final product SnS_2/MoS_2/3DG were confirmed via X-ray diffraction (XRD) as shown in Fig. 2c. The major peaks at 15.0°, 28.5°, and 32.2° are respectively indexed to the (001), (100), and (101) of SnS_2 (JCPDS No. 23-0677)[8,33], while the intense peak at 26.8° arises from the (002) crystal plane of graphitic carbon (JCPDS No. 75-1621)[29]. On the other hand, the new peaks at 34.3°, 38.0°, and 51.9° of the SnS_2/MoS_2/3DG can be assigned MoS_2 (JCPDS No. 65-3656)[34]. Raman spectroscopy was carried out to further identify the as-synthesized materials (Fig. 2d). The peak at 314 cm^{-1} is attributed to the A_{1g} mode of SnS_2[35], while the peaks at 378 and 405 cm^{-1} arises from the in-plane E^1_{2g} and out-of-plane A_{1g} modes of MoS_2[26,36]. In addition, the peaks at 1573 and 2718 cm^{-1} corresponds characteristic G and 2D bands of the 3DG[37,38]. Furthermore, the absence of the D band is indicative of the high quality and low defect of 3DG produced via CVD method[39]. Thermogravimetric analysis (TGA) was carried out, at a temperature range of 25 °C to 900 °C in dry air at a rate of 5 °C min^{-1}, to quantify the composition and verify the loading of MoS_2 on SnS_2/
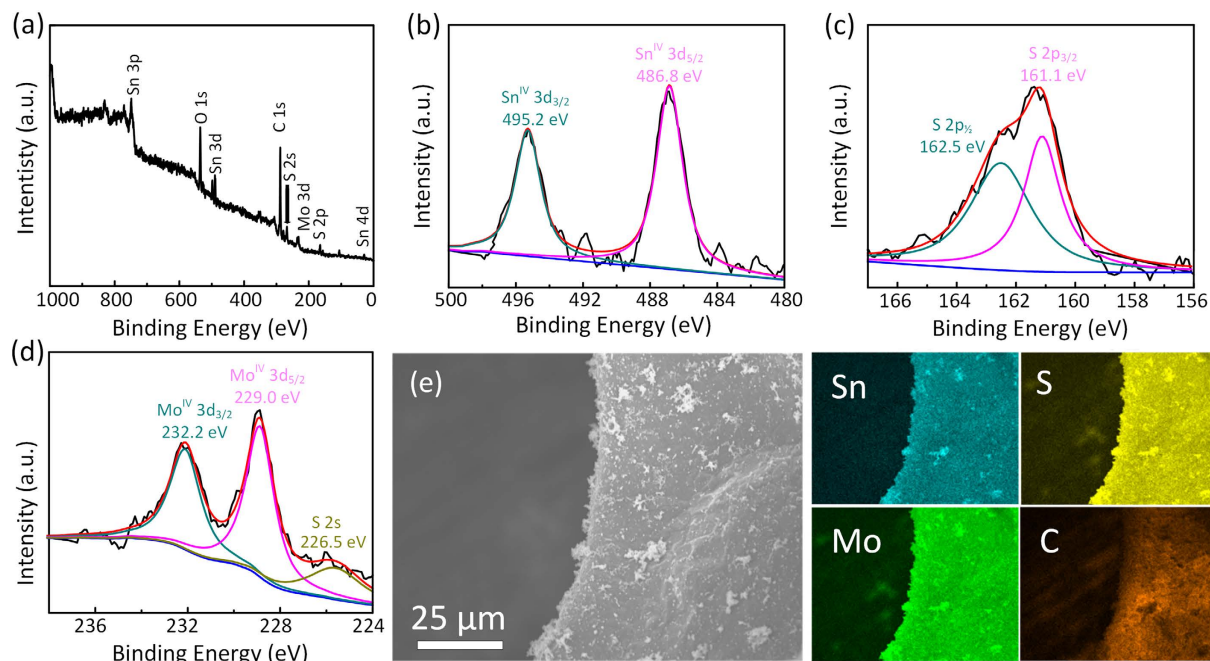
Figure 3. (**a**) XPS survey spectrum, (**b**) Sn 3d spectra, (**c**) S 2p spectra, and (**d**) Mo 3d spectra of SnS$_2$/MoS$_2$/3DG. (**e**) SEM image of SnS$_2$/MoS$_2$/3DG corresponding to the EDX elemental mapping images of Sn, S, Mo, and C showing uniform distribution of the elements.

MoS$_2$/3DG nanocomposite. From Figure S3, the initial weight loss of ~5% arises from the moisture loss from the surfaces of the samples. The second step between 200 to 500 °C is attributed to the oxidation of SnS$_2$ and MoS$_2$[28,40]. As SnS$_2$ and MoS$_2$ oxidize at roughly the same temperature range, mass loading of MoS$_2$ in SnS$_2$/MoS$_2$/3DG can be deduced by the difference in weight loss (~3%) between the two samples (SnS$_2$/3DG vs. SnS$_2$/MoS$_2$/3DG). Finally, the last weight loss step between 600 to 850 °C corresponds to the combustion of 3DG in air[29]. Therefore, based on TGA, the composition of SnS$_2$/MoS$_2$/3DG and be deduced to be SnS$_2$: 0.65, MoS$_2$: 0.03, 3DG: 0.32 [See supporting information for detailed derivation].

The chemical state and elemental distribution of SnS$_2$/MoS$_2$/3DG was also confirmed by X-ray photoelectron spectroscopy (XPS) and elemental dispersive X-ray (EDX) analysis, respectively. Figure 3a shows the broad spectrum of the XPS scan on SnS$_2$/MoS$_2$/3DG where the presence of elements Sn, S, Mo, and C are clearly observed. The high resolution XPS spectra of these elements are shown in Figs 3b,c,d, and S4, respectively. The deconvolution of these high resolution spectra produced pairs of peaks at 495.2 and 486.8 eV (Fig. 3b), 162.5 and 161.1 eV (Fig. 3c), and 232.2 and 229.0 eV (Fig. 3d), corresponding to the Sn 3d$_{3/2}$ and Sn 3d$_{5/2}$ states in SnS$_2$, S 2p$_{1/2}$ and S 2p$_{3/2}$ in MoS$_2$ and SnS$_2$, as well as Mo 3d$_{3/2}$ and Mo 3d$_{5/2}$ in MoS$_2$, respectively[22,41]. The results indicate the oxidation states of Sn and Mo to be +4, which are in good agreement with the phase pure results of SnS$_2$/MoS$_2$/3DG obtained via XRD. The deconvuluted C 1 s spectra in Figure S4 shows the presence of several oxygen functional groups on the surfaces of 3DG such as C-O/C-O-C at 285.2 eV as well as C=O/O-C=O at 288.5 eV[42]. In addition, EDX analysis in Fig. 3e shows homogenously distributed elements, Sn, Mo, S, and C, which implies the uniform growth of SnS$_2$/MoS$_2$ on the surfaces of 3DG.

Electrochemical Measurements. The catalytic effect of Mo in SnS$_2$/MoS$_2$/3DG was verified via electrochemical characterization through cyclic voltammetry (CV) and galvanostatic charge-discharge cycling. These experiments were carried out through the assembly of a half-cell battery with SnS$_2$/MoS$_2$/3DG as a binder-free electrode and lithium foil as a counter electrode. Control sample, SnS$_2$/3DG, was tested in the same conditions. Figure 4a shows the CV curves of the SnS$_2$/MoS$_2$/3DG electrodes. In the initial discharge cycle, the cathodic small broad peak centered at around 1.5 V can be attributed to the initial Li insertion into SnS$_2$ and MoS$_2$, without phase transformation, forming Li$_x$SnS$_2$ and Li$_x$MoS$_2$[9,43]. Upon further discharge, peaks at ~0.8 V and ~0.45 V can be ascribed to the conversion reaction of lithiated SnS$_2$ and MoS$_2$ to metallic Sn and Mo, respectively[16,43]. Towards the end of the discharge cycle, the broad peak from ~0.1–0.3 V corresponds to the alloying reaction between Sn and Li followed by the insertion of Li into 3DG, as well as the formation of the solid-electrolyte interface (SEI) film between the active materials and electrolyte. The formation of the SEI film contributes significantly to the initial loss in discharge capacity[9,29,44]. In the following charge-discharge cycles, the overlapping redox peaks can be attributed to the highly reversible lithium insertion/extraction, conversion and alloying reactions. The first redox pairs at ~0.1/0.25 V and ~1.2/1.3 V arise from the lithium insertion and extraction in 3DG and MoS$_2$, respectively[28,29]. Next, the alloying and de-alloying reactions of Sn with Li produces redox peaks centered around 0.25 V and 0.56 V, respectively[33]. Lastly, the redox pairs at ~1.16/1.86 V and ~1.8/2.26 V correspond to the conversion reactions occurring for both Sn and Mo, respectively[14,28]. In more details, the anodic peaks represent the
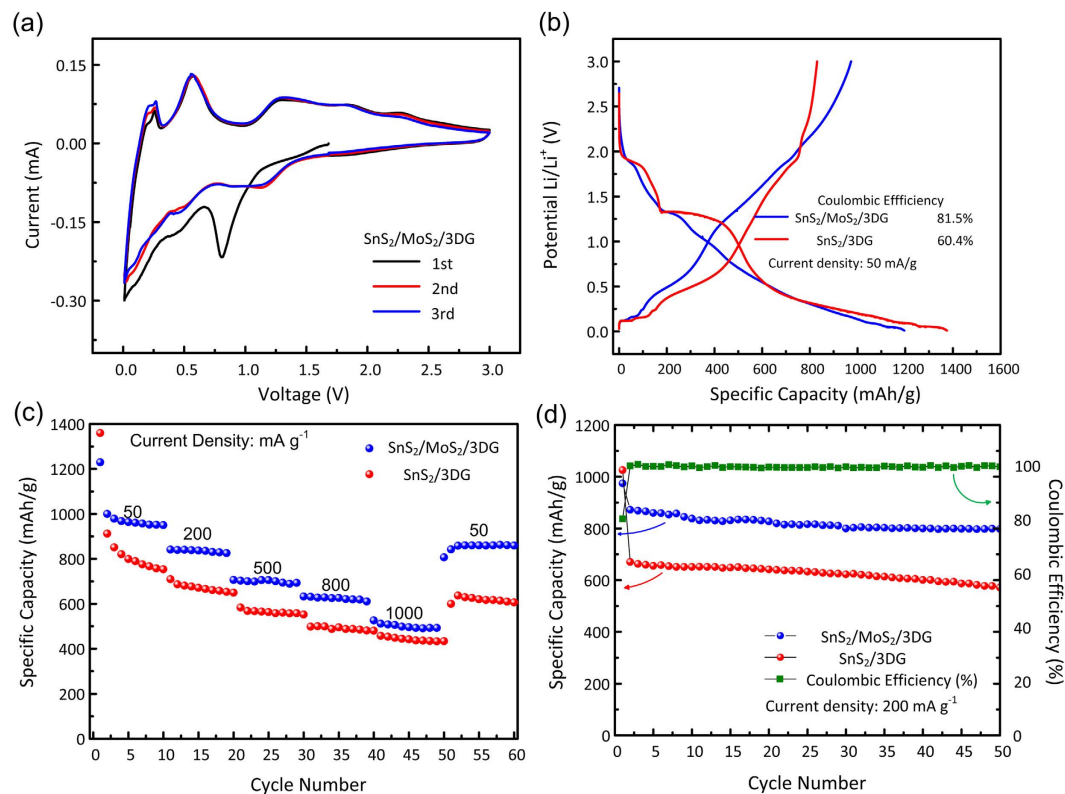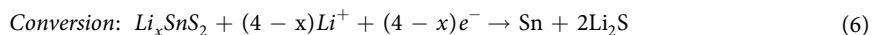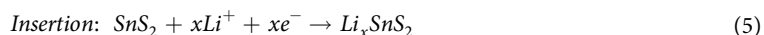
Figure 4. (**a**) Cyclic voltammograms of SnS₂/MoS₂/3DG electrode at a rate of 0.05 mV s⁻¹ in a potential range of 0.01 to 3.0 V. (**b**) Galvanostatic discharge and charge curves for SnS₂/MoS₂/3DG and SnS₂/3DG electrodes at the 1ˢᵗ cycle at a current density of 50 mA g⁻¹ in the potential range of 0.01 to 3.0 V showing the initial Coulombic Efficiency. (**c**) Rate capability of SnS₂/MoS₂/3DG and SnS₂/3DG electrodes. (**d**) Cycling performance of SnS₂/MoS₂/3DG and SnS₂/3DG electrodes at current density of 200 mA g⁻¹, and the corresponding coulombic efficiency of SnS₂/MoS₂/3DG electrode.

reduction of SnS_2 and MoS_2 to metallic Sn and Mo as well as formation of Li_2S. The cathodic peaks represent the reformation of SnS_2 and MoS_2 with the decomposition of Li_2S. In the absence of the catalyst, Mo, the CV curves of $SnS_2/3DG$ are similar to that of $SnS_2/MoS_2/3DG$ with the exception of the peaks arising MoS_2, as well as a gradually decaying redox pair ~1.32/1.87 V (Figure S5). The observed weakened redox pair indicates that the conversion reaction is only partially reversible in $SnS_2/3DG$. In contrast, the strong overlapping of the Sn conversion reaction redox pairs for $SnS_2/MoS_2/3DG$ implies that in the presence of Mo catalyst, the conversion process of Sn becomes highly reversible[14]. The reactions can be described using the following equations[9,28]:
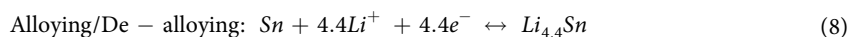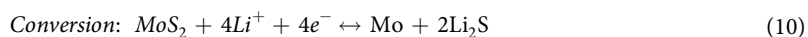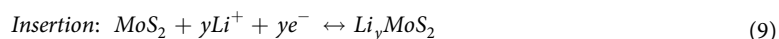
Reactions involving SnS_2

In the first discharge,

$$\text{Insertion: } SnS_2 + xLi^+ + xe^- \rightarrow Li_xSnS_2 \tag{5}$$

$$\text{Conversion: } Li_xSnS_2 + (4-x)Li^+ + (4-x)e^- \rightarrow Sn + 2Li_2S \tag{6}$$

Simplifying equations (5) & (6),

$$SnS_2 + 4Li^+ + 4e^- \rightarrow Sn + 2Li_2S \tag{7}$$

In subsequent charge-discharge cycles,

$$\text{Alloying/De-alloying: } Sn + 4.4Li^+ + 4.4e^- \leftrightarrow Li_{4.4}Sn \tag{8}$$

Reactions involving MoS_2

$$\text{Insertion: } MoS_2 + yLi^+ + ye^- \leftrightarrow Li_yMoS_2 \tag{9}$$

$$\text{Conversion: } MoS_2 + 4Li^+ + 4e^- \leftrightarrow Mo + 2Li_2S \tag{10}$$

Where x and y are the number of moles of Li$^+$/e$^-$ involved in the insertion reactions with SnS$_2$ and MoS$_2$ respectively.

Figure 4b shows the initial charge-discharge profile of both SnS$_2$/MoS$_2$/3DG and SnS$_2$/3DG. Similar to the CV curves, both electrodes display similar charge-discharge profile with differences owing to the presence of MoS$_2$ in SnS$_2$/MoS$_2$/3DG. The first discharge begins with a brief slope at ~1.8 V followed by a short plateau at ~1.3 V which is attributed to the insertion of Li ion (equations 5 & 9) into and subsequent conversion of SnS$_2$ and MoS$_2$ (equations 6 & 10), respectively[9,43]. Thereafter, the curve proceeds with a gentle slope towards 0.05 V followed by small plateau. The sloped region corresponds to the alloying process of Li with Sn (equation 8) as well as the formation of the SEI layer which results in an irrecoverable loss of lithium[9,44]. The small plateau at 0.05 V arises from the intercalation of Li ions to 3DG[29]. In the charge cycle, delithiation proceeds with extraction of Li ions from 3DG at ~0.15 V followed by de-alloying of Li$_{4.4}$Sn at ~0.5 V. Upon charging to higher voltage (1.0–3.0 V), Li$_x$MoS$_2$ delithiates (equation 9), Sn oxidizes to SnS$_2$ while Li$_2$S decomposes to S (backward reaction in equation 7)[14,43]. However, in the case of SnS$_2$/3DG, the oxidation of Sn and decomposition of Li$_2$S is limited, which can be observed in the acute slope between 1.9–3.0 V. Therefore, the catalytic effect of MoS$_2$ in SnS$_2$/MoS$_2$/3DG is evident with the reversible decomposition of Li$_2$S and oxidation of Sn to SnS$_2$ (equation 7). This is in stark contrast to previously reported SnS$_2$ electrodes where Li$_2$S formed during the initial discharge is irreversible or at most partially reversible in the first few cycles[9]. The reversible decomposition of Li$_2$S in the first cycle leads to an improved initial Coulombic Efficiency (ICE). This can be observed between the MoS$_2$ loaded, SnS$_2$/MoS$_2$/3DG with 81.5% CE (first discharge capacity: 1196.5 mA h g^{-1}, first charge capacity: 973.0 mA h g^{-1}) compared to SnS$_2$/3DG with 60.4% CE (first discharge capacity: 1372 mA h g^{-1}, first charge capacity: 829.7 mAh g^{-1}). The higher first discharge capacity in the SnS$_2$/3DG electrode may be due to a larger formation of SEI layer. The effective catalytic conversion reaction of SnS$_2$ may be attributed to the direct growth of MoS$_2$ on SnS$_2$ nanosheets that facilitate rapid reversible conversion process of Sn and decomposition of Li$_2$S.

Apart from improving the ICE, the reversible decomposition of Li$_2$S increases the total number of moles of Li ion reacting with SnS$_2$ from 4.4 (equation 8) to 8.4 (equations 7 and 8) by utilizing both alloying and conversion processes. In this manner, the theoretical capacity of SnS$_2$ increases significantly from 644 mA h g^{-1} (4.4 mols of Li$^+$) to 1231 mA h g^{-1}. In the case of SnS$_2$/MoS$_2$/3DG, the theoretical capacity of the nanocomposite, taking into the account of MoS$_2$ and 3DG, should be 940 mAh g^{-1} (Capacity$_{SnS2/MoS2/3DG}$ = 1231 * 0.65 + 670 * 0.03 + 372 * 0.32). This increase is evident even at different current densities as observed in Fig. 4c where the two different samples are subjected to galvanostatic charge-discharge cycles at increasing current densities. SnS$_2$/MoS$_2$/3DG delivered discharge capacities of 960.5, 837.0, 705.1, 626.2, and 495.6 mA h g^{-1} at current densities of 50, 200, 500, 800, and 1000 mA g^{-1}, respectively. This is distinctly higher as compared to SnS$_2$/3DG with highest reversible discharge capacities of ~800 mA h g^{-1} at low current densities of 50 mA g^{-1} and high current discharge capacity of 441.7 mA h g^{-1} at 1000 mA g^{-1}. Highly reversible and stable cycling was also observed for the MoS$_2$ loaded SnS$_2$/MoS$_2$/3DG at current density of 200 mA g^{-1} where capacity retention is 91.5% after 50 cycles (Fig. 4d). Furthermore, the first cycle CE is also consistent with that at 50 mA g^{-1} of 82% that increased and maintain near 100% in subsequent cycles (Fig. 4d). The high capacity, highly reversible and stable cycling implies the effective catalytic action of MoS$_2$. Furthermore, successful reversible decomposition of Li$_2$S at high current densities of 1000 mA g^{-1} highlights importance of the sandwiched MoS$_2$/SnS$_2$/MoS$_2$ nanostructure.

Electrochemical impedance spectroscopy (EIS) measurements were also conducted for both SnS$_2$/MoS$_2$/3DG and SnS$_2$/3DG to understand and evaluate the influence of MoS$_2$ loading on SnS$_2$/3DG. The measurements were performed on the samples at a semi-charged state (~2.5 V) across a frequency range of 10 mHz to 1 MHz.

Figure 5a shows the Nyquist plots where the curves from both electrodes display similar profile; a small semi-circle in the high frequency region corresponding to a combination of surface film resistance (R$_{sf}$) and charge transfer resistance (R$_{ct}$) followed by an acute straight line in the low frequency region which arises from the Warburg region (Z$_w$) as well as a Li accumulation element (C$_{int}$)[30,45]. An equivalent circuit consisting of R$_{sf+ct}$, Z$_w$, C$_{int}$, as well as R$_e$, which is the ohmic resistance arising from the electrolyte and cell components, and CPE$_{(sf+dl)}$, a constant phase element relating to the surface film and double layer, was used to fit the Nyquist plots (inset in Fig. 5a). The fitted values using the equivalent circuit are presented in Table S1. The lower surface film and charge transfer resistance (R$_{sf+ct}$) of SnS$_2$/MoS$_2$/3DG (33.65 Ω) compared to SnS$_2$/3DG (64.67 Ω) is an indication that MoS$_2$ loading improves charge kinetics. This improvement may be attributed to the release of conductive metallic Mo, through the conversion process of MoS$_2$ in the SnS$_2$/MoS$_2$/3DG electrode, over charge-discharge cycle. The effects of the enhanced conductivity via MoS$_2$ loading in SnS$_2$/MoS$_2$/3DG can be observed by evaluating the electrode at high current densities where charge kinetics are more demanding. Figure 5b shows the discharge capacities of SnS$_2$/MoS$_2$/3DG and SnS$_2$/3DG at high current densities of 1000 mA g^{-1} for 50 cycles where the capacity retention was 85.2%. Owing to the enhanced conductivity and charge kinetics, rapid catalytic action of Mo is achievable. This is reflected by the substantially increased capacity of the SnS$_2$/MoS$_2$/3DG (647 mA h g^{-1}) as compared to SnS$_2$/3DG (355.1 mA h g^{-1}) (Fig. 5b). Another key contributing factor to the effective catalytic action of Mo at different current densities is the well-designed SnS$_2$/MoS$_2$/3DG hierarchical nanostructure as illustrated in Fig. 5c. The sandwich MoS$_2$/SnS$_2$/MoS$_2$ nanostructure allows the released metallic Mo to be in direct proximity of Li$_2$S formed during lithiation. In this manner, Mo is able to rapidly catalyze the decomposition of Li$_2$S during delithiation.

Further evidence towards catalytic effect of Mo. In order to further demonstrate the catalytic effect of Mo, control samples of SnS$_2$ and SnS$_2$/MoS$_2$ were synthesized in the same method as SnS$_2$/3DG and SnS$_2$/MoS$_2$/3DG in the absence of 3DG, respectively. Without the 3DG current collectors to act as a platform for ordered growth, the as-synthesized SnS$_2$ nanosheets aggregated into micron sized clusters, which resembled a fully bloomed flower (Figure S6a). When MoS$_2$ was introduced, the nanosheets of MoS$_2$ was also able to grow on the surfaces of SnS$_2$ flowers (Figure S6b). Given the lack of a growth platform, the as-synthesized control samples
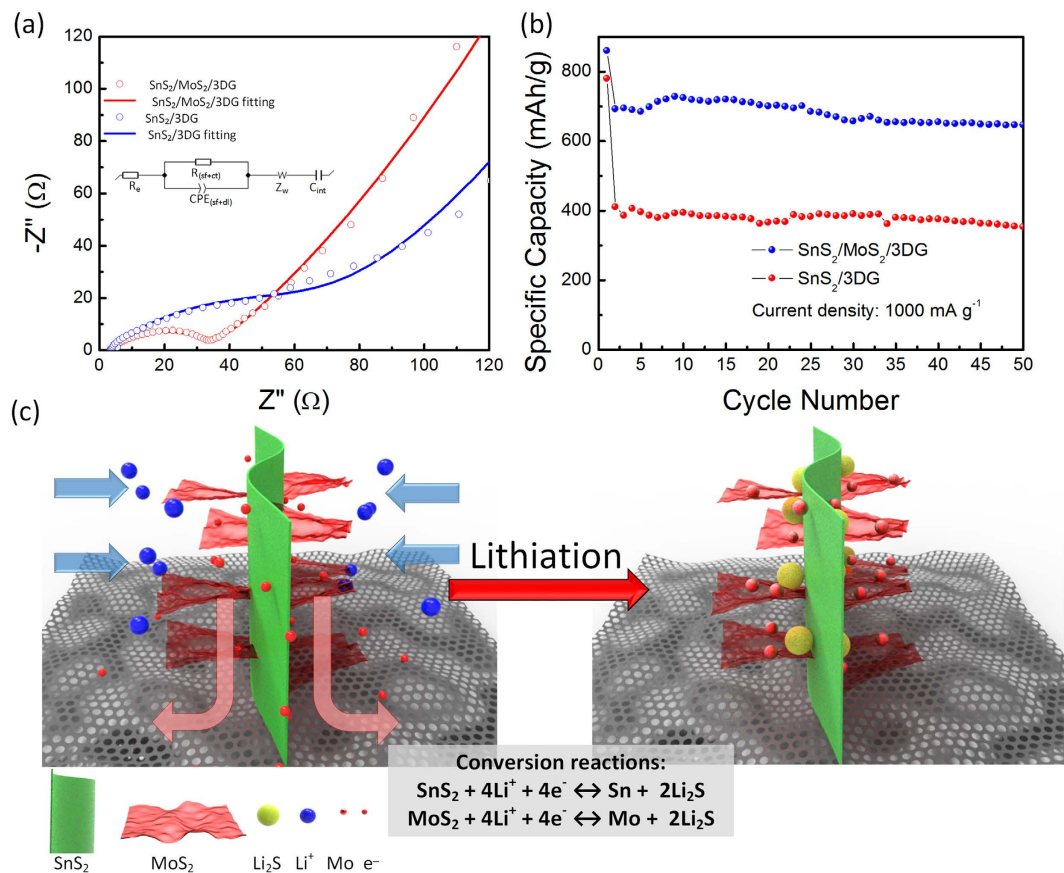
Figure 5. (**a**) Electrochemical impedance spectra of $SnS_2/MoS_2/3DG$ and $SnS_2/3DG$ electrodes as well as the corresponding fitting for both electrodes. Inset: Equivalent circuit used for curve fitting. (**b**) Cycling performance of $SnS_2/MoS_2/3DG$ and $SnS_2/3DG$ electrodes at current density of $1000\,mA\,g^{-1}$. (**c**) Illustration of $MoS_2/SnS_2/MoS_2$ sandwich structure which is able to efficiently promote catalytic action.

were in the form of powders. Hence, to obtain an electrode, these powders were made into a slurry form that were subsequently coated on Ni-foam current collectors and finally assembled into coin cells. Similarly, CV and galvanostatic cycling were performed on SnS_2 and SnS_2/MoS_2 as shown in Figure S6c–f. The CV peaks of SnS_2 and SnS_2/MoS_2 are consistent with $SnS_2/3DG$ and $SnS_2/MoS_2/3DG$, respectively, with the exception of peaks arising from 3DG. In terms of galvanostatic cycling, the catalytic effect could also be observed in SnS_2/MoS_2 where there is a significant improved of ICE from 55% (SnS_2) to 67% (SnS_2/MoS_2) (Figure S6e) as well as improved discharge capacity from $6745\,mAh\,g^{-1}$ (SnS_2) to $806\,mAh\,g^{-1}$ (SnS_2/MoS_2) (Figure S6f). However, at higher current densities (500, 800, and $1000\,mA\,g^{-1}$), both electrodes delivered roughly the same discharge capacities. This could be due to the instability of the SnS_2/MoS_2 structure that resulted in the gradual dissociation of MoS_2 nanosheets from SnS_2 surfaces because of significant volume changes of SnS_2 after prolonged cycling. Therefore, these results further supports the presence of the catalytic action of Mo towards the decomposition of Li_2S and oxidation of Sn to SnS_2 which results in a substantial improvement towards both the ICE and capacities of SnS_2 anodes. Furthermore, despite the improvement, the rapid decay in capacities of SnS_2/MoS_2 highlights the importance of a rational design towards a well-structured composite that is demonstrated in $SnS_2/MoS_2/3DG$.

Thus far, there has already been numerous reports citing high discharge capacities in SnS_2-based anode beyond its $644\,mAh\,g^{-1}$ theoretical capacity[14–21]. In most of these cases, SnS_2 was synthesized as a nanocomposite together with reduced graphene oxide (rGO). For example, Lin *et al.* reported the synthesis of ultrasmall SnS_2 on rGO with high capacities of $1034\,mA\,h\,g^{-1}$ at current density of $64.5\,mA\,g^{-1}$ while few-layer $SnS_2/$graphene presented by Chang *et al.* delivered capacities of $920\,mA\,h\,g^{-1}$[16,46]. However, the contributing factors towards the excess capacity are loosely assigned to a synergistic effect between SnS_2 and rGO without clear clarification. In a recent report, Qu *et al.* attributed the high capacities of the $SnS_2/$Graphene nanocomposite to a reversible conversion of SnS_2 from Sn through a catalytic effect brought about by Sn nanoparticles, which were released during conversion reactions of SnS_2, stacked within graphene matrices[14]. Unfortunately, there was no physical evidence provided to support this postulation. Furthermore, due to the presence of defects, surface functional groups and other additional Li storage sites, the capacity of rGO varies depending on the quality of the graphene sheets and can be as high as $\sim 1000\,mA\,h\,g^{-1}$[47]. As a result, the capacity contribution by rGO in the $SnS_2/$rGO nanocomposites may be more significant than reported.

In an analogous system, the reversible decomposition and formation of Li_2O from SnO_2 and GeO_2 has been shown to be mediated in the presence of nano-sized catalyst, Co and Ge respectively. This led to capacities beyond
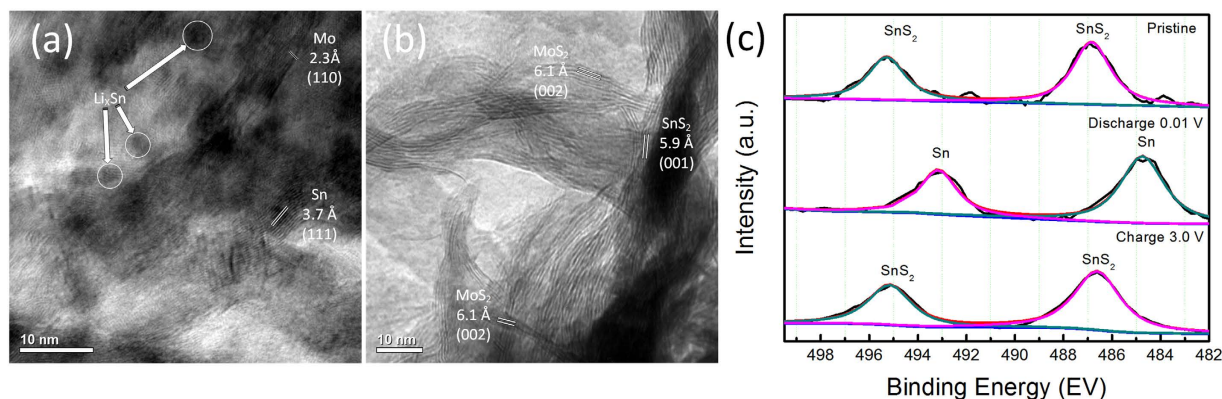
Figure 6. *Ex situ* **analysis of post cycled SnS₂/MoS₂/3DG electrode.** HRTEM image of (**a**) discharge (0.01 V) state and (**b**) charge (3.0 V) state. (**c**) Sn 3d spectra of the electrode in pristine, discharge, and charge state.

their theoretical capacities (SnO₂/Co₃O₄/rGO: 1038 mAh g⁻¹ vs SnO₂: 782 mAh g⁻¹ and GeO₂/Ge/C: 1860 mAh g⁻¹ vs GeO₂: 1126 mAh g⁻¹)[48–52]. The enhanced capacities were attributed to the catalytic role of the respective dopants which facilitated the reversible formation and decomposition of Li_2O. Another consequence of this catalytic effect is the improvement of initial Coulombic efficiencies (ICE) as a significant portion of the initial capacity is typically lost due to the formation of irreversible Li_2O apart from the formation of surface electrolyte interface (SEI). Therefore, since SnS_2 is analogous to SnO_2, the effect of the catalyst can be extended to SnS_2 based anodes.

The reversible oxidation/reduction of SnS_2/Sn and Li/Li_2S as described in equation 7 occurs during the discharge/charge cycles, respectively. Hence, evidence of the reversibility of equation 7 can be investigated through the detection of the products at the end of discharge (0.01 V) and charge (3.0 V) process. In this regard, post cycling TEM and XPS was conducted for SnS_2/MoS₂/3DG electrodes after 20 cycles at current density of 200 mA g⁻¹. Being free from additives such as binder and active carbon, the cycled electrodes were free from stray and unwanted signals in the post cycling characterizations. Two sets of coin cells were cycled with one set ending at full discharge state (0.01 V) and the other at full charge state (3.0 V). The electrodes were extracted from the coin cell in the Ar-filled glove box, soaked overnight with acetonitrile and washed with ethanol several times. The *ex-situ* HRTEM of the fully discharged and charged electrodes are shown in Fig. 6a,b, respectively. Upon full discharge (lithiation), crystalline lattices corresponding to metallic Mo and Sn can be found (Fig. 6a). This corresponds to the conversion process of MoS_2 and SnS_2 to their metallic phases as well as the incomplete lithium alloying of Sn[51,53,54]. On the other hand, lithiated Sn alloy (Li_xSn) which are often reported as nanoparticles embedded within the Sn-based electrodes, may be identified as the dark nanoparticles (~3–5 nm) circled out in Figs 6a and S7[55–57]. However, crystal lattice of the Li_xSn nanoparticles could not be clearly observed as they are embedded within the overlapping lattices from Sn and Mo in the complicated SnS_2/MoS₂/3DG structure. Li_2S was not identified due to its amorphous nature at full lithiated state[58]. In the fully charged state (delithiation), the presence of crystalline lattices which can be assigned to MoS_2 and SnS_2, implies a reversible conversion process of metallic Mo and Sn as well as Li_xSn to their intial state (Fig. 6b). Therefore, Sn formed in the discharge state and SnS_2 charged state corresponds well with reversibility of equation 7 where the forward reaction corresponds to discharge (formation of Sn) and backward reaction the charge process (formation of SnS_2). As an additional evidence towards the reversible conversion of SnS_2, *ex-situ* XPS was also conducted on the cycled electrodes at full discharge and charge states. Figure 6c compares the high-resolution XPS spectra of SnS_2/MoS₂/3DG electrodes at different states, pristine, discharged to 0.01 V, and charged to 3.0 V. The pristine electrode corresponds to the initial state of SnS_2/MoS₂/3DG where the XPS spectra peaks corresponds to Sn $3d_{5/2}$ and Sn $3d_{3/2}$ as discussed in Fig. 3b. Upon discharge, these peaks shift downwards to 493.1 eV and 484.7 eV corresponding the reduction of Sn^{4+} of SnS_2 to metallic tin (Sn^0)[59]. In the charge state, the shifted peaks returns to the initial positions of 495.1 eV and 486.6 eV indicating an oxidation of Sn^0 to Sn^{4+}, i.e. the reformation of SnS_2[60]. Once again, the presence of Sn at discharge states and SnS_2 at charged states points towards the reversibility of the reaction in equation 7. Therefore, the results obtained from the *ex-situ* HRTEM and XPS analyses of the post cycled electrodes at charged and discharge states provides conclusive evidence that the reversible conversion reactions of SnS_2 (equation 7) are promoted through the catalytic action of transition metal, Mo, in the active material matrix.

Conclusion

In summary, a rationally designed hierarchical nanostructured SnS_2/MoS₂/3DG nanocomposite was synthesized via stepwise solovothermal synthesis of metal sulfides on a lightweight current collector substrate, 3DG. The stepwise synthesis facilitated the growth of self-assembled vertical SnS_2 nanosheets on surfaces of 3DG followed by growth of ultrafine MoS_2 nanosheets which branches out on both sides of SnS_2, creating a sandwich MoS_2/SnS_2/MoS₂ structure. The sandwich structure places MoS_2 in very close proximity to SnS_2 that facilitates rapid catalytic action of Mo towards decomposition of Li_2S and conversion of SnS_2. As a catalyst towards the reversible conversion reaction of SnS_2, the loading of MoS_2 on SnS_2/MoS₂/3DG was controlled at a low content of 3%. A small amount of Mo proved sufficient towards the catalytic effect reversible conversion of SnS_2 that saw a significantly improved ICE as well as increased discharge capacities even up to high current density of 1000 mA g⁻¹. The binder-free SnS_2/MoS₂/3DG lightweight electrode also facilitated post cycling investigations. *Ex situ* HRTEM

and XPS analysis of charged and discharged electrodes provided substantial evidence towards the catalytic effect of Mo in the reversible conversion of SnS_2; metallic Sn and Mo could be found in discharged electrodes while SnS_2 and MoS_2 identified in charged electrodes. Therefore, the use of catalyst to unlock the potential of SnS_2 as an anode that exploits both conversion and alloying reactions creates a new direction towards high capacity metal sulfide anode materials.

Experimental Section

$SnS_2/MoS_2/3DG$ was prepared by 3 general steps 1, chemical vapor deposition (CVD) to obtain 3DG 2, solvothermal to obtain SnS_2 on 3DG ($SnS_2/3DG$), and 3 solvothermal to obtain MoS_2 on $SnS_2/3DG$ ($SnS_2/MoS_2/3DG$).

Preparation of 3DG and removal of Ni Foam. The preparation of the 3DG foam adopts a similar method as previously reported[29,33,61]. Ni foam (1.6 mm thick, purchased from Alantum Advanced Technology Materials (Shenyang)) was cut into 150 mm × 45 mm pieces. The rectangular Ni foam pieces are then rolled and placed into a 1 inch quartz tube. Before heat was applied, Argon (Ar) gas was allowed to flow for 10 mins to remove residual air in the tube. Thereafter, a heat rate of 50 °C min^{-1} was applied to heat the quartz tube to 1000 °C. At this temperature, ethanol vapour was mixed with the flowing N_2/H_2 gas through the bubbling of anhydrous ethanol. The mix N_2/H_2/ethanol vapour was allowed to flow for 5 mins. Lastly, the quartz tube was allowed to cool to room temperature rapidly (~100 °C/min). The Ni foam on 3DG-Ni was removed in an etchant solution of 3 M HCl at 80 °C. Pure 3DG was washed using deionized (DI) water and ethanol several times before drying at 60 °C. The typical loading of this process yields ~0.5 mg cm^{-2} of 3DG on Ni foam (3DG-Ni).

Synthesis of $SnS_2/3DG$. The synthesis of $SnS_2/3DG$ follows the previously reported method with the addition of SDS[33]. SnS_2 grown on 3DG ($SnS_2/3DG$) was prepared via a simple solvothermal reaction. $SnCl_4 \cdot 5H_2O$ (32 mM), thioacetamide (TAA) (80 mM), and Sodium dodecyl sulfate (SDS) (0.07 mM) was weighed and dissolved into 35 mL ethanol. Magnetic stirring and mild heat (50 °C) was applied to ensure homogeneity of the precursors. 6 pieces of 3DG (12 mm diameter) was cut and together with the mixture, transferred into a 50 mL Teflon-line stainless steel autoclave. The reaction proceeded by heating the autoclave at 180 °C for 12 h. After the reaction, as-synthesized $SnS_2/3DG$ was collected by rinsing with DI H_2O and ethanol, and drying at 60 °C. The loading of SnS_2 on 3DG was ~1.2 mg. Control sample, pristine SnS_2, was synthesized by the same method in the absence of 3DG.

Synthesis of $SnS_2/MoS_2/3DG$. $SnS_2/3DG$ synthesized in the previous step was used directly in this step after drying at 60 °C. MoS2 grown on $SnS_2/3DG$, termed as $SnS_2/MoS_2/3DG$, was prepared by an L-cysteine assisted solvothermal reaction. L-cysteine (0.25 mM) and $Na_2MoO_4 \cdot 2H_2O$ (0.03 mM) was weighed and dissolved in 15 mL DI H_2O. 15 mL of ethanol was added to the continuously stirred mixture. 6 pieces of $SnS_2/3DG$ was added to the mixture and transferred to a 50 mL Teflon-line stainless steel autoclave. The stainless steel autoclave was heated at 180 °C for 12 h. The as-synthesized $SnS_2/MoS_2/3DG$ was collected by rinsing with DI H_2O and ethanol, and drying at 60 °C. The loading of MoS_2 on $SnS_2/3DG$ was between 0.05–0.1 mg. Lastly, the $SnS_2/MoS_2/3DG$ was annealed in Nitrogen (N_2) environment at 400 °C for 2 hours at a slow heating rate of 3 °C min^{-1}. Control sample, SnS_2/MoS_2, was synthesized following the above method using pristine SnS_2 in place of $SnS_2/3DG$.

Materials Characterization. The nanostructures and morphology of the as-synthesized samples were imaged under a field-emission scanning electron microscope (FESEM, JSM-7600) and transmission electron microscope (TEM, JEM-2100F). Crystalline phase and structure of the samples were identified by X-ray diffraction (XRD, Bruker D8). Raman spectroscopy was conducted by a confocal Raman setup with a 532 nm lazer excitation (WITec Instruments Corp, Germany). The nanocomposite content breakdown was measured by thermogravimetric analysis (TGA, Shimadzu, DTG-60). The chemical valence states of the samples were investigated with a X-ray photoelectron spectroscope (XPS, PHI Quantera II, Physical Electronics, Adivision of ULCAV-PHI).

Coin cell assembly and Electrochemical measurements. The as-synthesized $SnS_2/MoS_2/3DG$ was used directly as an anode in the two electrode half-cell configuration where lithium metal acts as the counter electrode (cathode). Control samples of $SnS_2/3DG$, pristine SnS_2, and SnS_2/MoS_2 were also assembled. Pristine SnS_2 was synthesized using the procedure described in step 2, in the absence of 3DG whereas SnS_2/MoS_2 was synthesized using the procedure described in step 3 by using pristine SnS_2 instead of $SnS_2/3DG$. Electrodes for the powdered control samples, SnS_2 and SnS_2/MoS_2 were made into a slurry and subsequently coated on Ni foam current collectors (12 mm diameter each). The slurry was prepared by mixing 8 parts of active materials to 1 part of polyvinylidene fluoride (PVDF) binder and 1 part of carbon black in the presence of N-Methylpyrrolidone (NMP) solvent. The $SnS_2/3DG$ was used directly as an electrode. All working electrodes were dried at 120 °C for 12 h before assembly. The coin cell were assembled in an Ar-filled glove box using standard CR 2032 as casing. Each cell consisted of a Celgard 2400 membrane sandwiched between a working electrode (active material) and counter electrode (lithium metal). Electrolyte used was a mixture of 1 M LiPF6 solution in Ethylene Carbonate (EC)/Di-Methyl Carbonate (DMC), 1:1 v/v. Electrochemical measurements, cyclic voltammetry (CV) and electrochemical impedance spectroscopy (EIS) were performed using an electrochemical workstation (VMP3, Biologic, France). While galvanostatic charge-discharge cycles were carried out using a battery analyser (Neware, China).

References

1. M. Armand & J.-M. Tarascon, Building better batteries. *Nature* **451,** 652–657 (2008).
2. B. Dunn, H. Kamath & J. M. Tarascon, Electrical energy storage for the grid: a battery of choices. *Science* **334,** 928–935 (2011).
3. J.-M. Tarascon & M. Armand, Issues and challenges facing rechargeable lithium batteries. *Nature* **414,** 359–367 (2001).
4. M. N. Obrovac & V. L. Chevrier, Alloy negative electrodes for Li-ion batteries. *Chem. Rev.* **114,** 11444–11502 (2014).

5. C. M. Park, J. H. Kim, H. Kim & H. J. Sohn, Li-alloy based anode materials for Li secondary batteries. *Chem. Soc. Rev.* **39,** 3115–3141 (2010).

6. M. V. Reddy, G. V. Subba Rao & B. V. Chowdari, Metal oxides and oxysalts as anode materials for Li ion batteries. *Chem. Rev.* **113,** 5364–5457 (2013).

7. X. Xu, W. Liu, Y. Kim & J. Cho, Nanostructured transition metal sulfides for lithium ion batteries: Progress and challenges. *Nano Today* **9,** 604–630 (2014).

8. J. W. Seo *et al.* Two-Dimensional SnS$_2$ Nanoplates with Extraordinary High Discharge Capacity for Lithium Ion Batteries. *Adv. Mater.* **20,** 4269–4273 (2008).

9. T.-J. Kim, C. Kim, D. Son, M. Choi & B. Park, Novel SnS$_2$-nanosheet anodes for lithium-ion batteries. *J. Power Sources* **167,** 529–535 (2007).

10. T. Momma *et al.* SnS$_2$ anode for rechargeable lithium battery. *J. Power Sources* **97,** 198–200 (2001).

11. H. S. Kim, Y. H. Chung, S. H. Kang & Y.-E. Sung, Electrochemical behavior of carbon-coated SnS$_2$ for use as the anode in lithium-ion batteries. *Electrochim. Acta* **54,** 3606–3610 (2009).

12. M. He, L.-X. Yuan & Y.-H. Huang, Acetylene black incorporated three-dimensional porous SnS$_2$ nanoflowers with high performance for lithium storage. *RSC Adv.* **3,** 3374–3383 (2013).

13. J.-G. Kang *et al.* Three-dimensional hierarchical self-supported multi-walled carbon nanotubes/tin(iv) disulfide nanosheets heterostructure electrodes for high power Li ion batteries. *J. Mater. Chem.* **22,** 9330 (2012).

14. B. Qu *et al.* Origin of the Increased Li$^+$-Storage Capacity of Stacked SnS$_2$/Graphene Nanocomposite. *Chem Electro Chem* **2,** 1138–1143 (2015).

15. L. Zhuo *et al.* One-step hydrothermal synthesis of SnS$_2$/graphene composites as anode material for highly efficient rechargeable lithium ion batteries. *RSC Adv.* **2,** 5084 (2012).

16. L. Mei *et al.* Superior electrochemical performance of ultrasmall SnS$_2$ nanocrystals decorated on flexible RGO in lithium-ion batteries. *J. Mater. Chem. A* **1,** 8658–8664 (2013).

17. M. Zhang *et al.* Graphene oxide oxidizes stannous ions to synthesize tin sulfide–graphene nanocomposites with small crystal size for high performance lithium ion batteries. *J. Mater. Chem.* **22,** 23091 (2012).

18. D. Kong *et al.* A novel SnS$_2$@graphene nanocable network for high-performance lithium storage. *RSC Adv.* **4,** 23372 (2014).

19. S. Liu *et al.* Preferential c-Axis Orientation of Ultrathin SnS$_2$ Nanoplates on Graphene as High-Performance Anode for Li-Ion Batteries. *ACS Appl. Mater. Interfaces* **5,** 1588–1595 (2013).

20. M. Sathish, S. Mitani, T. Tomai & I. Honma, Ultrathin SnS$_2$ Nanoparticles on Graphene Nanosheets: Synthesis, Characterization, and Li-Ion Storage Applications. *J. Phys. Chem. C* **116,** 12475–12481 (2012).

21. Y. Zhu *et al.* Tucked flower-like SnS$_2$/Co$_3$O$_4$ composite for high-performance anode material in lithium-ion batteries. *Electrochim. Acta* **190,** 843–851 (2016).

22. Y. Du *et al.* A facile, relative green, and inexpensive synthetic approach toward large-scale production of SnS$_2$ nanoplates for high-performance lithium-ion batteries. *Nanoscale* **5,** 1456–1459 (2013).

23. Q. Wu *et al.* One-pot synthesis of three-dimensional SnS$_2$ hierarchitectures as anode material for lithium-ion batteries. *J. Power Sources* **239,** 89–93 (2013).

24. Z. Ma *et al.* Flexible hybrid carbon nanotube sponges embedded with SnS$_2$ from tubular nanosheaths to nanosheets as free-standing anodes for lithium-ion batteries. *RSC Adv.* **6,** 30098–30105 (2016).

25. X. Jiang *et al.* *In situ* assembly of graphene sheets-supported SnS$_2$ nanoplates into 3D macroporous aerogels for high-performance lithium ion batteries. *J. Power Sources* **237,** 178–186 (2013).

26. Y. Shi *et al.* Self-assembly of hierarchical MoSx/CNT nanocomposites (2<x<3): towards high performance anode materials for lithium ion batteries. *Sci. Rep.* **3,** 2169 (2013).

27. Y. Wang *et al.* Core-leaf onion-like carbon/M$_n$O$_2$ hybrid nano-urchins for rechargeable lithium-ion batteries. *Carbon* **64,** 230–236 (2013).

28. Y. Wang *et al.* Pre-lithiation of onion-like carbon/MoS$_2$ nano-urchin anodes for high-performance rechargeable lithium ion batteries. *Nanoscale* **6,** 8884–8890 (2014).

29. Z. X. Huang *et al.* 3D graphene supported MoO2 for high performance binder-free lithium ion battery. *Nanoscale* **6,** 9839–9845 (2014).

30. Z. X. Huang, Y. Wang, J. I. Wong, W. H. Shi & H. Y. Yang, Synthesis of self-assembled cobalt sulphide coated carbon nanotube and its superior electrochemical performance as anodes for Li-ion batteries. *Electrochim. Acta* **167,** 388–395 (2015).

31. A. Chakrabarti *et al.* Tin(IV) sulfide: Novel nanocrystalline morphologies. *Inorganica Chimica Acta* **374,** 627–631 (2011).

32. J. Gajendiran & V. Rajendran, Synthesis of SnS$_2$ nanoparticles by a surfactant-mediated hydrothermal method and their characterization. *Adv. Nat. Sci.: Nanosci. Nanotechnol.* **2,** 015001 (2011).

33. Z. X. Huang, Y. Wang, J. I. Wong & H. Y. Yang, Free standing SnS$_2$ nanosheets on 3D graphene foam: an outstanding hybrid nanostructure anode for Li-ion batteries. *2D Materials* **2,** 024010 (2015).

34. L. Yang *et al.* Porous metallic MoO2-supported MoS$_2$ nanosheets for enhanced electrocatalytic activity in the hydrogen evolution reaction. *Nanoscale* **7,** 5203–5208 (2015).

35. C. Wang, K. Tang, Q. Yang & Y. Qian, Raman scattering, far infrared spectrum and photoluminescence of SnS$_2$ nanocrystallites. *Chem. Phys. Lett.* **357,** 371–375 (2002).

36. Y. Shi *et al.* MoS$_2$ Surface Structure Tailoring via Carbonaceous Promoter. *Sci. Rep.* **5,** 10378 (2015).

37. H. Ji *et al.* Ultrathin Graphite Foam: A Three-Dimensional Conductive Network for Battery Electrodes. *Nano Lett.* **12,** 2446–2451 (2012).

38. D. Chao *et al.* A V2O5/Conductive-Polymer Core/Shell Nanobelt Array on Three-Dimensional Graphite Foam: A High-Rate, Ultrastable, and Freestanding Cathode for Lithium-Ion Batteries. *Adv. Mater.* **26,** 5794–5800 (2014).

39. Z. Chen *et al.* Three-dimensional flexible and conductive interconnected graphene networks grown by chemical vapour deposition. *Nat. Mater.* **10,** 424–428 (2011).

40. C. Zhai, N. Du, H. Zhang, J. Yu & D. Yang, Multiwalled carbon nanotubes anchored with SnS$_2$ nanosheets as high-performance anode materials of lithium-ion batteries. *ACS Appl. Mater. Interfaces* **3,** 4067–4074 (2011).

41. L. Wang, Y. Ma, M. Yang & Y. Qi, One-pot synthesis of 3D flower-like heterostructured SnS$_2$/MoS$_2$ for enhanced supercapacitor behavior. *RSC Adv.* **5,** 89069–89075 (2015).

42. W. Liu, C. Lu, X. Wang, K. Liang & B. K. Tay, *In situ* fabrication of three-dimensional, ultrathin graphite/carbon nanotube/NiO composite as binder-free electrode for high-performance energy storage. *J. Mater. Chem. A* **3,** 624–633 (2015).

43. J. Wang *et al.* MoS$_2$ architectures supported on graphene foam/carbon nanotube hybrid films: highly integrated frameworks with ideal contact for superior lithium storage. *J. Mater. Chem. A* **3,** 17534–17543 (2015).

44. J. B. Goodenough & K. S. Park, The Li-ion rechargeable battery: a perspective. *J. Am. Chem. Soc.* **135,** 1167–1176 (2013).

45. D. Aurbach, Review of selected electrode–solution interactions which determine the performance of Li and Li ion batteries. *J. Power Sources* **89,** 206–218 (2000).

46. K. Chang *et al.* Few-layer SnS$_2$/graphene hybrid with exceptional electrochemical performance as lithium-ion battery anode. *J. Power Sources* **201,** 259–266 (2012).

47. D. Pan *et al.* Li Storage Properties of Disordered Graphene Nanosheets. *Chem. Mater.* **21,** 3136–3142 (2009).

48. K. H. Seng, M. H. Park, Z. P. Guo, H. K. Liu & J. Cho, Catalytic role of Ge in highly reversible GeO$_2$/Ge/C nanocomposite anode material for lithium batteries. *Nano Lett.* **13,** 1230–1236 (2013).
49. Y. G. Zhu *et al.* Catalyst engineering for lithium ion batteries: the catalytic role of Ge in enhancing the electrochemical performance of SnO$_2$(GeO$_2$)0.13/G anodes. *Nanoscale* **6,** 15020–15028 (2014).
50. J. Hwang *et al.* Mesoporous Ge/GeO$_2$/Carbon Lithium-Ion Battery Anodes with High Capacity and High Reversibility. *ACS Nano* **9,** 5299–5309 (2015).
51. Y. Wang *et al.* Designed hybrid nanostructure with catalytic effect: beyond the theoretical capacity of SnO$_2$ anode material for lithium ion batteries. *Sci. Rep.* **5,** 9164 (2015).
52. C. H. Kim, Y. S. Jung, K. T. Lee, J. H. Ku & S. M. Oh, The role of *in situ* generated nano-sized metal particles on the coulombic efficiency of MGeO3 (M=Cu, Fe, and Co) electrodes. *Electrochim. Acta* **54,** 4371–4377 (2009).
53. J. R. Dahn, I. A. Courtney & O. Mao, Short-range Sn ordering and crystal structure of Li4.4Sn prepared by ambient temperature electrochemical methods. *Solid State Ionics* **111,** 289–294 (1998).
54. S. K. Das, R. Mallavajula, N. Jayaprakash & L. A. Archer, Self-assembled MoS$_2$–carbon nanostructures: influence of nanostructuring and carbon on lithium battery performance. *J. Mater. Chem.* **22,** 12988 (2012).
55. A. Nie *et al.* Atomic-Scale Observation of Lithiation Reaction Front in Nanoscale SnO$_2$ Materials. *ACS Nano* **7,** 6203–6211 (2013).
56. C. M. Wang *et al. In situ* transmission electron microscopy observation of microstructure and phase evolution in a SnO(2) nanowire during lithium intercalation. *Nano Lett.* **11,** 1874–1880 (2011).
57. Y. Lu & E. Fong, Biomass-mediated synthesis of carbon-supported nanostructured metal sulfides for ultra-high performance lithium-ion batteries. *J. Mater. Chem. A* **4,** 2738–2745 (2016).
58. L. Wang, Z. Xu, W. Wang & X. Bai, Atomic mechanism of dynamic electrochemical lithiation processes of MoS(2) nanosheets. *J. Am. Chem. Soc.* **136,** 6693–6697 (2014).
59. M. He *et al.* A SnO$_2$@carbon nanocluster anode material with superior cyclability and rate capability for lithium-ion batteries. *Nanoscale* **5,** 3298–3305 (2013).
60. R. Hu *et al.* Dramatically enhanced reversibility of Li$_2$O in SnO$_2$-based electrodes: the effect of nanostructure on high initial reversible capacity. *Energy Environ. Sci.* **9,** 595–603 (2016).
61. Y. G. Zhu *et al.* Phase Transformation Induced Capacitance Activation for 3D Graphene-CoO Nanorod Pseudocapacitor. *Adv. Energy Mater.* **4,** 1301788 (2014).

Acknowledgements

Author Contributions

Z.X.H. and H.Y.Y. conceived the idea and design the project. Z.X.H. carried out material synthesis and electrochemical tests. Y.W., B.L., D.K., J.Z. and T.C. contributed to the material characterizations and batteries analysis. All authors contributed to the writing of the manuscript. All the authors discussed the results and commented on the manuscript. H.Y.Y. supervised the project.

Additional Information

Supplementary information accompanies this paper at http://www.nature.com/srep

Competing financial interests: The authors declare no competing financial interests.

How to cite this article: Huang, Z. X. *et al.* Unlocking the potential of SnS$_2$: Transition metal catalyzed utilization of reversible conversion and alloying reactions. *Sci. Rep.* **7,** 41015; doi: 10.1038/srep41015 (2017).

Publisher's note: Springer Nature remains neutral with regard to jurisdictional claims in published maps and institutional affiliations.